Journal of Materials Chemistry A

Accepted Manuscript

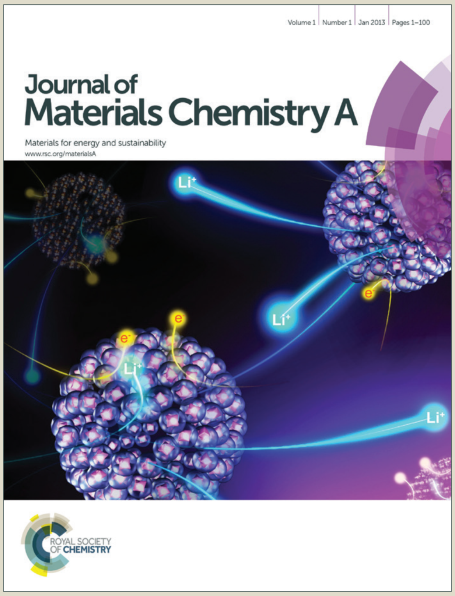

ROYAL SOCIETY OF CHEMISTRY

www.rsc.org/materialsA

New Cu_xS_y/nanoporous carbon composites as efficient oxygen reduction catalysts in alkaline medium

Mykola Seredych,[1] Enrique Rodriguez-Castellon,[2] and Teresa J. Bandosz[1*]

[1]Department of Chemistry, The City College of New York,160 Convent Ave, New York, NY, 10031, USA.

[2]Departamento de Química Inorgánica, Facultad de Ciencias, Universidad de Málaga, Spain.

[*]Whom Correspondence should be addressed to. E-mail: tbandosz@ccny.cuny.edu; Tel: (212) 650-6017; Fax : (212) 650-6107

Graphical content entry

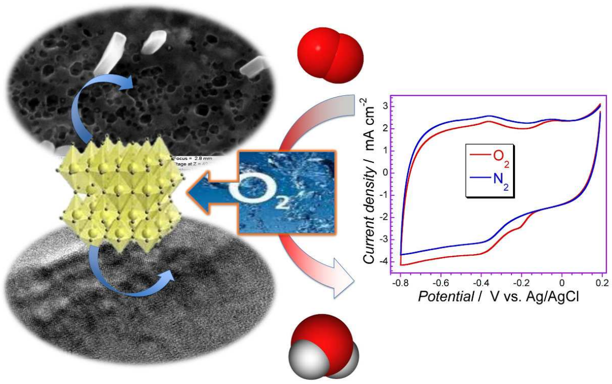

Hybrid Cu_xS_y/S-doped nanoporous carbon composite is a superior non-noble metal catalyst for the oxygen-reduction reaction (ORR). The unique surface features of the material resulted in a marked catalytic activity for ORR in alkaline medium, high tolerance to methanol oxidation and long term stability.

Summary

A new hybrid catalyst containing crystalline copper-based phases, Cu_xS_y, CuO, $Cu_4(OH)_6SO_4$ and S-doped nanoporous polymer-derived carbon was obtained by carbonization of the physical mixture of Cu-BTC (MOF)/graphite oxide composites with a commodity polymer (Poly(4-styrenesulfonic acid-co-maleic acid) sodium salt). The resulting highly porous composites with a high degree of mesoporosity compared to the initial carbon showed a marked electrocatalytic activity for oxygen reduction reaction (ORR) in alkaline medium. The current density was higher than that on commonly used platinum modified carbon and number of electron transfer (~ 4ē) indicated the high efficiency for ORR. This was accompanied by a high tolerance to methanol oxidation and superior long-term stability after 1500 potential cycles. The extensive surface characterization (XPS, XRD, SEM/EDX, HR-TEM and nitrogen adsorption) indicated the fast O_2 adsorption and charge transfer owing to the surface hydrophobicity, small pores, and conductivity. The synergistic effect of crystalline copper-based phases and S-doped carbon leads to high ORR activity and high kinetic current densities.

Keywords: copper/graphene/nanoporous carbon, composites, sulfur, surface chemistry, electrocatalysis, oxygen reduction reaction

1. Introduction

Efficient oxygen reduction under fuel cell working conditions is an important technological process, which needs to be addressed towards solving the contemporary energy problem. So far Pt/C based cathodes are commercially used for these important catalytic reactions.[1, 2] Nevertheless, they suffer a low tolerance to fuel cross over and their production is associated with the extensive cost of the noble metal providing catalytic properties. Therefore improving the performance of non-noble metal electrocatalysts towards the reduction of oxygen is a research target of many academic and industrial centers.[3-17]

One group of catalysts which is widely investigated for oxygen reduction reactions (ORR) are heteroatom doped nanoporous carbons[16-25] and other carbonaceous materials such as graphene oxide or graphene.[3, 4, 6, 7-10, 12, 16] Even though the important features of these materials are a high electrical conductivity, high surface area and efficient charge transfer, of paramount significance is the presence of heteroatoms such as nitrogen,[5, 6, 8, 9, 11, 15, 20, 21, 25] sulfur,[6, 7, 10, 12, 16] phosphorus,[18, 23, 24] or boron.[23, 26, 27] They are doped to the graphene layers and their presence in aromatic rings changes the properties of a carbon surface providing sites for oxygen adsorption and reduction.[3, 10, 12, 26] In this group of materials, so far the highest number of electron transfer (n) and high density of the kinetic- current (J_k) were reported on metal free N-doped porous carbon by Li and coworkers.[28] The calculated values from Koutecky–Levich plot were n = 3.96 and J_k = 4.02 mA cm^{-2} at -0.50 V vs. SCE (0.51 V vs. RHE). For sulfur and nitrogen dual-doped mesoporous graphene electrocatalyst these values were n = 3.3 and J_k = 24.5 mA cm^{-2} at -0.50 V vs. Ag/AgCl (0.48 V vs. RHE).[10] These materials also showed the high tolerance to methanol cross over.[10, 28] Nevertheless, in the majority of studies the ORR follows an incomplete 4ē electron pathway at more positive potential.[29] Recently, it has been demonstrated that N-doped mesoporous carbon (N-MC) is highly active as ORR catalyst and has durability of the bifunctional air electrodes for hybrid Li-air batteries and other metal-air batteries.[30] Its higher current density compared to commercial Pt/C at a more negative potential was indicated as an advantage in hybrid Li–air batteries with a wide range of operating voltage.[30]

Another research path explored in the development of efficient ORR catalysts is that based on non precious metal oxides and nanoparticles. Here examples are carbon materials containing Fe, Co, Mn, Ni, Cu oxides and nanoparticles.[14, 17, 20, 21, 31, 32] They are known to favor the four-electrons transfer mechanism. Nevertheless, their activity still does not match that of Pt/C.[3, 20, 31] These metal oxides, to provide promising performance, need to be engineered to certain sizes, shapes, and structures. Their homogenous distribution on the surface of the carbon support is also a challenge.[32] Recently, An and coworkers synthesized carbon-supported CoN/C nanoparticles, which exhibited high ORR activity and has comparable onset potential (0.85 V vs. RHE) to that of commercial Pt/C.[17]

Recently, metal organic frameworks containing such metals as copper,[33] cobalt[34] and iron[35] were indicated as precursors of ORR catalysts. Their high temperature pyrolysis, owing to the presence of an organic phase resulted in new composites of improved properties.[34, 36-38] Their ORR performance could be further enhanced by an addition of a graphene phase providing faster path for electron transfer reactions.[38] The highest kinetic current density reported on these materials reached 8.8 mA cm^{-2} with 4 electrons transfer path at -0.4 V vs. Ag/AgCl (0.58 V vs.

RHE).[38] Moreover, the high tolerance to methanol cross over was also reported and compared to that of a commercial Pt/C catalyst (20 wt. % Pt on Vulcan XC-72, dp < 5 nm for Pt).[38]

Copper is a promising non precious metal catalyst for ORR. There have been reported various oxidative reactions catalyzed by different copper complexes and oxides.[39, 40] Moreover, studies by Jahan and coworkers and Qiao and coworkers have indicated a marked performance of CuO/Gr composites for ORR.[33, 41] Recently, we have shown a promising performance of the copper/graphene phase catalysts obtained from Cu-BTC/graphite oxide composites.[38] The unique architecture of copper particles on graphene sheets, combined with a high electrical conductivity and surface hydrophobicity led to the catalyst showing high electrocatalytic activity and tolerance to methanol cross over with a 4ē reduction path.[38]

Following the copper-focused line of research, and combining this with our experience in the development of Cu-BTC/GO composites[42] and electrochemically active sulfur doped nanoporous carbons,[43] the objective of this paper is to address the excellent performance of a new ORR catalyst obtained from the precursors consisting composite of Metal Organic Frameworks (MOF) with graphite oxide (GO)[42] and commodity sulfur containing polymer (Poly(4-styrenesulfonic acid-co-maleic acid) sodium salt). An advance compared to state-of-the-art in this field is in producing a catalyst of a developed surface area, high conductivity and in combining the catalytic activity of sulfur doped carbon with copper oxide/sulfide nanoparticles. The application of MOF in electrocatalysis has been scarcely explored, due to their intrinsic poor electron conductive properties and limited charge transfer.[33, 35, 44] Some attempts to partially overcome this limitation have considered hybrid MOF composites prepared by adding a conductive phase; for instance, Jahan and co-workers[33] have recently reported a graphene oxide/Cu-MOF composite with enhanced electrocatalytic properties for ORR and hydrogen and oxygen evolution reactions. Still these materials underperform the activity of Pt/C based catalysts.[6, 10, 11] Another MOF, Co-based imidazolate framework, was used as a carbonization precursor for ORR catalysts by Ma and coworkers.[34] The observed catalytic activity was linked to the coordination of cobalt with nitrogen owing to the specific chemistry of the organic linkages.

In our approach we use the materials derived by heat treatment of copper-based MOF HKUST-1/graphite oxide (GO) composite[42] in the presence of a carbon phase as an electrocatalyst for ORR in alkaline medium. The presence of the graphene phase in the carbon/copper composites resulted in unique surface features of the catalyst, reducing character of the carbon component, and enhanced electrical conductivity. A highly distributed copper catalyst is expected to enhance an electron transfer within the well developed micro/mesoporous carbon texture and to provide hydrophobicity enhancing oxygen adsorption. To stress the importance of the specific chemical and structural nature of the copper/carbon/graphene composite, the surface features and the performance of the new electrocatalysts are compared to those of a catalyst obtained by heat treatment of the precursor polymer itself and to those of Vulcan Pt containing carbon.

2. Experimental Section

2.1. Materials

The preparation of the copper based MOF, Cu-BTC,[45] graphite oxide (GO) and their composite with 46 wt. % of GO has been addressed in details previously.[42] Briefly, the GO was suspended into the solution of the chemicals used to synthesize MOF and following the procedure described for Cu-BTC synthesis.

Poly(4-styrenesulfonic acid-co-maleic acid) sodium salt was used as a nanoporous carbon precursor.[46] The powdered polymer was carbonized at 800 ^{o}C (heat rate 50 °C min^{-1}) for 40 min under nitrogen (300 mL min^{-1}). This sample is referred to as CPS. The polymer composites with copper were synthesized by mixing the amount of polymer corresponding to 90 or 80 % of resulting nanoporous carbons (calculated taking into account the yield of CPS carbon) with 10 or 20 % of the composite MOF/GO (this corresponds to concentration 64.7 mg$_{GO}$ mL^{-1} DMF) (calculated taking into account the yield of MOF/GO at 800 ^{o}C), respectively. Then the mixture was carbonized under nitrogen at 800 °C for 40 min. The resulting carbon with copper was washed in water in a Soxhlet apparatus to remove an excess of water-soluble inorganic salts. The resulting catalysts are referred to as CPS-Cu10 and CPS-Cu20 where numbers 10 and 20 represent the percentage of the composite MOF/GO added to the polymer (10 or 20 %, respectively). The performance of the samples was compared to that of a commercial Pt/C catalyst (20 wt. % Pt on Vulcan XC-72, dp < 5 nm for Pt, Sigma-Aldrich).

2.2. Methods

Electrochemical Characterization: The performance of our materials for electrochemical ORR was investigated in 0.1 M KOH using a three-electrode cell with Ag/AgCl/KCl (3 M) as a reference electrode. The measurements of chronoamperometry and long term stability by applying 1500 potential cycles were carried out on VersaSTAT MC (AMETEK, Princeton Applied Research) with a scanning rate of 5 mV s^{-1} (cyclic voltammetry). The working electrode was prepared by mixing the active material with polyvinylidene fluoride (PVDF) and commercial carbon black (carbon black, acetylene, 50 % compressed, Alfa Aesar) (8:1:1) in N-methyl-2-pyrrolidone (NMP) until homogeneous slurry. The slurry was coated on a Ti foil (current collector) with the total surface area of 1 cm^2 of an active material. Linear sweep voltammograms were obtained in 0.1 KOH using 757 VA Computrace (Metrohm) at various rotation rates (from 0 to 2000 rpm) with Ag/AgCl (3 M KCl) and Pt wire as a reference and a counter electrode, respectively. The measurements of cyclic voltammetry were carried out under O_2 or N_2 saturation in the electrolyte in the potential range of 0.19 to -0.8 V vs. Ag/AgCl (1.17 V to 0.18 V vs. RHE) at a scan rate of 5 mV s^{-1}. The working electrode was prepared by dispersing 2 mg of the catalyst in 1 ml of deionized water and 0.5 ml of 1 wt. % Nafion aqueous solution. About 5 μl of the prepared slurry was dropped (three times) on a polished glass carbon electrode (Metrohm, Switzerland, diameter 2 mm) and dried at 50 ºC in air. The potential was swept from 0.19 to -0.8 V vs. Ag/AgCl (1.17 V to 0.18 V vs. RHE) at a scan rate of 5 mV s^{-1}. After each scan, the electrolyte was saturated with air (the source of O_2) for 20 minutes. All the experiments were carried out at a room temperature.

RHE conversion

The measured potentials versus the Ag/AgCl (3M KCl) reference electrode were converted to the reversible hydrogen electrode (RHE) scale using Nernst equation:

$$E_{RHE} = E_{Ag/AgCl} + 0.059pH + E^{o}{}_{Ag/AgCl}$$

where E_{RHE} is the converted potential versus RHE, $E_{Ag/AgCl}$ is the experimental potential measured against the Ag/AgCl reference electrode, and $E^{o}{}_{Ag/AgCl}$ is the standard potential of Ag/AgCl (3 M KCl) at 25 °C (0.210 V). The electrochemical measurements were carried out in 0.1 M KOH (pH = 13) at room temperature; therefore, $E_{RHE} = E_{Ag/AgCl} + 0.977$ V.

X-ray diffraction (XRD): XRD measurements were conducted using standard powder diffraction procedures analyzed by CuK$_\alpha$ radiation (tension – 40 kV and current – 40 mA) generated in a Phillips X'Pert X-ray diffractometer. The scan rate used was 2.3 deg min^{-1}.

Scanning electron microscopy (SEM): SEM images were performed at Zeiss Supra 55 VP. The accelerating voltage was 5.00 kV. Scanning was performed in situ on a sample powder without coating. Electron-dispersive X-ray spectroscopy (EDX) analysis was done at magnification 5 KX with an accelerating voltage 15.00 kV and the content of elements on the surface was calculated.

Transmission electron microscopy (TEM): TEM was performed on a Zeiss EM 902 instrument. The microscope has a line resolution of 0.34 nm and a point resolution of 0.5 nm and operates in normal diffraction, and low dose modes at 50 or 80 kV. High-resolution transmission electron microscopy (HR-TEM) was performed on a JEOL 2100 LaB6 instrument operating at 200 kV. Analyses were performed after the samples were dispersed in ethanol.

Evaluation of porosity: Sorption of nitrogen at its boiling point was carried out using ASAP 2020 (Micromeritics, Surface Area and Porosity Analyzer). Before the experiments, samples were out-gassed at 120 °C to constant vacuum (10^{-4} Torr). The surface area, S_{BET}, (Brunauer-Emmet-Teller method was used) and S_{NLDFT}, the micropore volume, V_{mic}, the mesopore volume, V_{mes}, the total pore volume, V_t, (calculated from the last point of the isotherms based on the volume of nitrogen adsorbed). The volume of mesopores, V_{mes}, represents the difference between total pore and micropore volume. The relative microporosity was calculated as the ratio of the V_{mic} and V_t. The S_{NLDFT}, volume of pores and pore size distribution were calculated using 2D-NLDFT (www.NLDFT.com) assuming the heterogeneity of the pore sizes. [47]

Evaluation of hydrophobicity level: The hydrophobicity level of our samples was determined using their affinity to adsorb water and benzene. Predetermined amounts of dry samples were exposed either to water or benzene vapors in air-tight environments for 24 hours at room temperature. The amounts adsorbed were measured gravimetrically using a TA instrument thermal analyzer (SDT Q 600). The weight loss in nitrogen between 30 and 120 °C was assumed as an equivalent to the quantity of water or benzene adsorbed on the surface. The hydrophobicity level (HL) is defined as the ratio of the amount of benzene adsorbed to that of water.

X-ray photoelectron spectra (XPS) analysis: XPS analysis were collected using a Physical Electronics PHI 5700 spectrometer with nonmonochromatic Mg K_α radiation (300 W, 15 kV, 1253.6 eV) for the analysis of the core level signals of C 1*s*, O 1*s* S 2*p* and Cu 2*p* and with a multichannel detector. Spectra of powdered samples were recorded with the constant pass energy values at 29.35 eV, using a 720 µm diameter analysis area. Under these conditions, the Au $4f_{7/2}$ line was recorded with 1.16 eV FWHM at a binding energy of 84.0 eV. The spectrometer energy scale was calibrated using Cu $2p_{3/2}$, Ag $3d_{5/2}$, and Au $4f_{7/2}$ photoelectron lines at 932.7, 368.3, and 84.0 eV, respectively. The PHI ACCESS ESCA-V6.F software package was used for acquisition and data analysis. A Shirley-type background was subtracted from the signals. Recorded spectra were always fitted using Gauss–Lorentz curves, in order to determine the binding energy of the different element core levels more accurately. The error in BE was estimated to be ca. 0.1 eV. A first acquisition was performed with 8 min of irradiation time only to avoid as much as possible the photo-reduction of Cu(II) species. Nevertheless, a Cu(II) reduction in high vacuum during the analysis cannot be excluded.[48]

DC conductivity measurements: The DC conductivity was measured using a 4-probe method on the pellets with the composition 90 wt. % of copper/graphene/carbon materials and 10 wt. % polytetrafluoroethylene as binder. The prepared composition was pressed by a Carver Press machine applying 2 tons pressure and disk-shaped well-packed pellets with diameter 8 mm were formed. The pellets were dried in oven for 12 hours. The pellets' thickness was measured by a spring micrometer. The measurement of conductivity was carried out using the Keithley 2400 Multimeter.

Thermal analysis-mass spectroscopy (TA-MS) and inorganic matter content: Thermogravimetric (TG) curves were obtained using a TA instrument thermal analyzer (SDT Q 600), which was connected to a gas analysis system (OMNI Star^{TM}) mass spectrometer. The samples were heated up to 1000 ^{o}C (10 ^{o}C min^{-1}) under a constant helium flow (100 mL min^{-1}). From the TG curves, differential TG (DTG) curves were derived. The composition of gases was measured by MS and gas evolution profiles as a function of temperature were evaluated. The inorganic phase content was determined by burning the samples in air up to 1000 ºC.

3. Results and Discussion

3.1. Electrochemical performance in alkaline solution

The comparison of the CV curves for the samples studied is presented in Fig. 1. They are obtained after equilibration and saturation of the solution of the electrolyte either with air (O_2) or with nitrogen (N_2). All samples show the capacitive behavior and the electrochemical capacitance increases with an increase of the amount of copper/Cu-BTC MOF in the catalyst precursor. No leaching of copper was detected. An increase in anodic current at the end of the potential window is likely related to the oxidation of carbon functional groups in reduced forms. An interesting feature, which appears only when oxygen is present in the electrolyte is the hump at 0.73 V vs. RHE (Fig. 1). Since it is not observed in an absence of oxygen we link it to ORR. Once again, more copper in the sample results in an increase in the measured cathodic current at this potential. The other humps visible on CV curves (cathodic at 0.60 V and anodic at 0.63 V and 0.93 V vs. RHE are linked to redox reaction of copper.[49, 50] Thus redox anodic peaks are due to Cu(0)/Cu(I)/Cu(II) transitions. Peak at 0.60 V corresponds to the oxidation Cu to Cu(I) and peak at 0.93 V is related to the formation of Cu(II) species (oxides/hydroxides)[49, 50] following either a one (Cu_2O to Cu(II) or two step reaction (direct Cu to Cu(II). Interestingly, in the cathodic range, besides the obvious peak related to oxygen reduction reactions, only one redox peak at 0.63 V related to the reduction of Cu(II) or two step process is seen.[49-51] Lack or reduction of Cu_2O (expected at about 0.28 V vs. RHE) indicates an absence of this species on the surface of our materials and thus a direct reduction of Cu(II) to Cu(0) at 0.63 V. The CV curves for the composites suggest a similar speciation of copper on the surface of both composites.

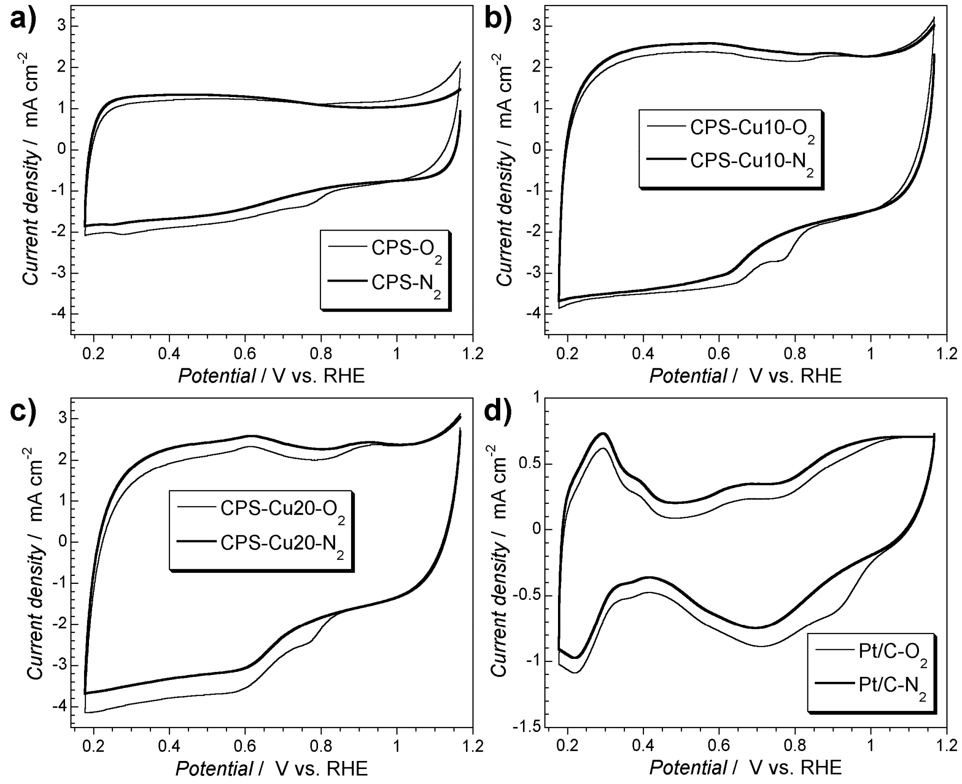

Fig. 1. Cyclic voltammograms on modified glassy carbon RDE in air-saturated 0.1 M KOH at scan rate of 5 mV s^{-1} for the (a) polymer-derived carbon, (b and c) copper/carbon composites and (d) 20% Pt on Vulcan XC-72.

Linear scan voltammetry experiments (Fig. 2) were run to determine the current density related to ORR and the number of electron transfer. The LSV results were corrected for capacitive currents contribution. The corresponding onset potentials for CPS, CPS-Cu10, CPS-Cu20 and Pt/C are 0.812 V, 0.823 V, 0.835 V and 0.947 V vs. RHE, respectively. The same onset potential value for commercial Pt/C was found by Liang and coworkers.[10] Thus an increase in the copper content in the composite visibly improves the performance of the catalysts for ORR resulting in a positive shift in the onset potential. These values are comparable to those obtained on the copper –containing catalyst based on MOF/GO composite without an addition of the carbon phase.[38] The onset potential values are also similar to those reported for CuO/r-NGO,[41] Cu-MOF/GO composites[33] and some metal-free doped graphene materials.[10] Nevertheless, they still do not reach the onset potential reported for Pt/C.[10, 38]

The difference in the behavior of our catalyst and Pt/C is also in the shape of the diffusion limiting plateau which exhibits a slope non exiting for the latter sample. The reason for this might be is in much higher porosity of our materials than that of Pt/C Vulcan XC-72 whose surface area was reported as 150 m^2/g.[52] The presence of small pores can limit the mass transport. This effect were discussed by Bang and coworkers in their study of carbon-based for direct methanol fuel cell electrodes.[53]

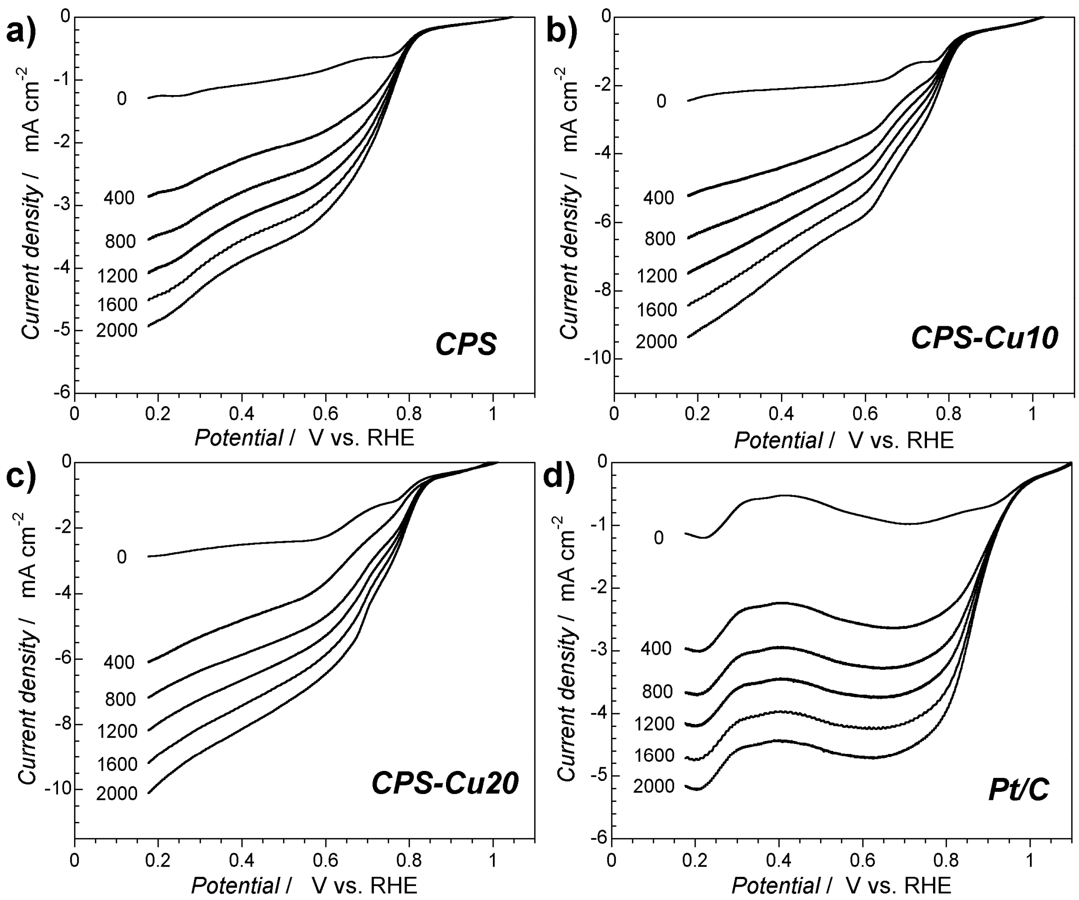

Fig. 2. Linear sweep voltammograms on modified glassy carbon RDE in air-saturated 0.1 M KOH at different rotation speeds and scan rate of 5 mV s^{-1} for the (a) polymer-derived carbon, (b and c) copper/carbon composites and (d) 20% Pt on Vulcan XC-72. LSV for oxygen reduction reaction was corrected for capacitive currents contribution.

To calculate the number of electron transfer, Koutecky–Levich plots were constructed (Fig. S1 of ESI) and the calculated from them the numbers of electron transfer and kinetic current densities in the potential range between 0.68 and 0.18 V vs. RHE are compared in Fig. 3. Even though the polymer derived carbon shows some activity with *n* between 1.4 and 2.1, the composites with copper visibly outperform the carbon showing a very efficient electron transfer process (*n* between 3 and 4) almost in the whole potential range. In analyzing the number of electron transfer the contribution from redox copper transition has to be taken into account at the more positive potential than 0.58 V. Nevertheless, at potential 0.73 V where ORR can be clearly separated from reduction of copper the number of electron transfer is at around 3.0 and 1.6 electrons greater than that on the carbon without copper. At 0.73 V there is practically no differences in the performance between two composites studied. However, at more negative potential where copper redox transitions start to play a role composite with more copper in its composition outperforms its counterpart with less copper.

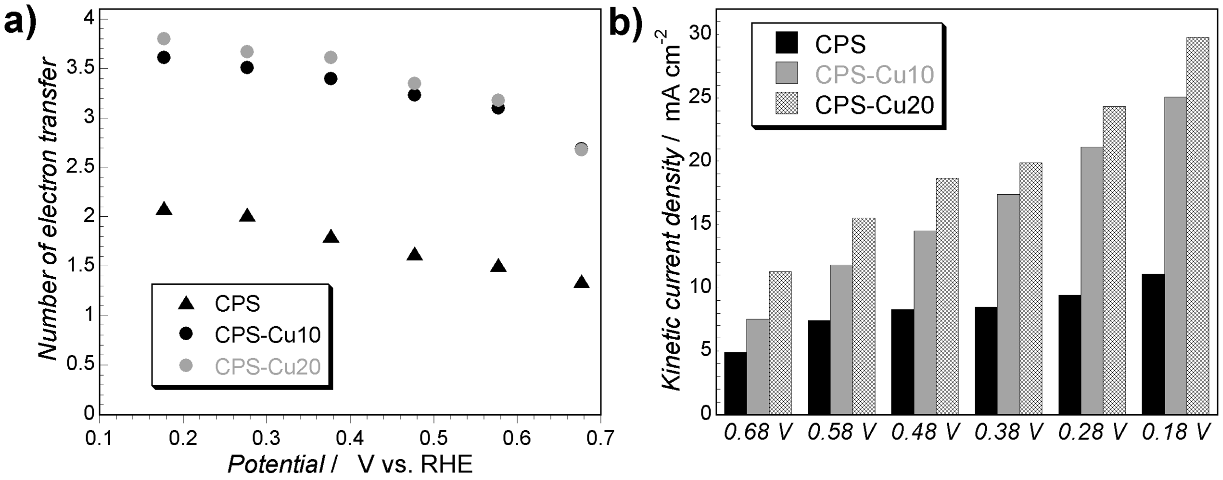

Fig. 3. a) Number of electron transfer versus potential; b) comparison of the kinetic current density.

The difference between the composites are seen when the calculated kinetic current densities are compared (Fig. 3b). The kinetic current density generated on the catalysts is about 100 % higher than that on the CPS carbon and varies between 12-30 mA cm^{-2} in the potential range between 0.68 V to 0.18 V vs. RHE. An increase in the amount of copper has a profound effect on the kinetic current density at more positive potential range where at 0.68 V the 30 % difference between CPS-Cu10 and CPS-Cu20 is found. At more negative potentials the current on CPS-

Cu20 is about 15% greater than that on CPS-Cu10. Even though copper redox transitions can affect the kinetic current density at the more negative potential than 0.58 V that marked difference measured at the more positive potential suggests that the copper species play an important role in catalyzing ORR. The values measured at the potential of 0.68 V are comparable to those measured on copper oxide/N-doped reduced graphene oxide reported by Qiao and coworkers[41] and higher than those for cuprous oxide nanoparticles dispersed on reduced graphene oxide.[54] The kinetic current densities measured at 0.18 V are 29.8 and 25.1 mA cm^{-2} for CPS-Cu20 (n = 3.8) and CPS-Cu10 (n = 3.7), respectively. These values are higher than those obtained for other Cu- [33, 54] Co- [34] and Fe- based [20, 35] catalysts and some metal-free carbons.[25, 28] In analyzing the magnitude of the kinetic current we have to remember that air was a source of oxygen for ORR and only about 8 mg L^{-1} of O_2 can be dissolved in ambient conditions in comparison with 36 mg L^{-1} when pure oxygen is used. This limitation led to a smaller current than that expected when electrolyte is saturated with the pure oxygen, as reported often in the literature.[55] The calculated from Koutecky–Levich plot kinetic current density at 0.68 V for CPS-Cu20 is twice higher than that for the initial nanoporous carbon, indicating the better performance of the former sample (Fig. 3a). It’s important to mention that the kinetic current density for the CPS-Cu20 is higher (~ 10 %) compared to that on the Vulcan XC-72. This high current density at more negative potential can be beneficial in hybrid Li–air batteries with a wide range of operating voltage.[30]

To further test the applicability of our materials as ORR catalysts in alkaline medium, the tolerance to methanol crossover was assessed at 0.73 V vs. RHE (Fig. 4a and Fig. 5b) where the cathodic reduction of O_2 was detected (Fig. 1). The chronoamperometry was first run under N_2

saturation of the electrolyte and then air was purged through the system. A sharp increase in the cathodic current was measured for all samples. After stabilization of the current, three separate spikes of methanol (0.2 mL) were injected to the electrolyte. As seen from Fig. 4a the current remained unchanged showing the high tolerance of these materials towards methanol oxidation. This tolerance is better than that measured on a commercial 20 wt. % Pt/C Vulcan XC-72where significant shift in current from cathodic to a reversed anodic has been measured after methanol injection (Fig. 5b).[6, 10, 11, 38]

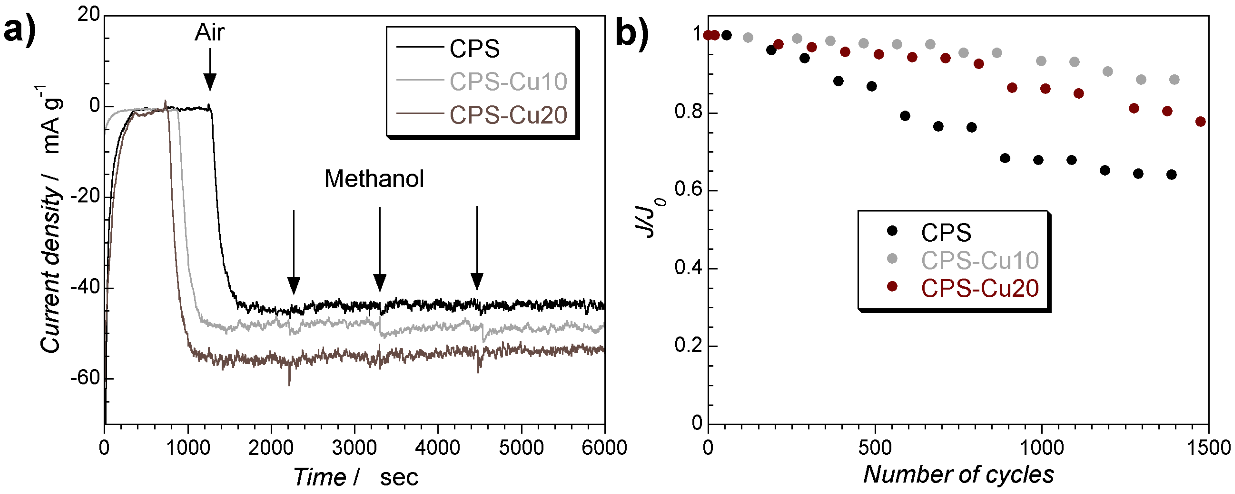

Fig. 4. a) Chronoamperometry for methanol tolerance at the potential 0.73 V; b) Stability testing by cycling at 0.73 V.

The long term stability of the electrocatalytic activity of our materials was tested by exposing them to 1500 cycles and after each 100 cycles the ORR current was determined at 0.73 V vs. RHE (Fig. 4b). The copper containing composites are much more stable than the polymer derived carbon and a decrease in the measured ORR current after 1500 cycles was 20 % for CPS-Cu20 and 12 % for CPS-Cu10. For the carbon itself the current decrease was close to 40 %. The higher stability of CPS-Cu10 is an interesting finding in the light of its higher number of electron transfer than that for CPS-Cu20 at 0.73 V. To explain these differences and to understand the role of copper and surface chemistry in general, the detailed surface characterization of the materials studied was carried out. Various techniques of surface evaluation were used since not only chemistry but also textural and electrical features of the materials are important for their catalytic performance.[1, 3]

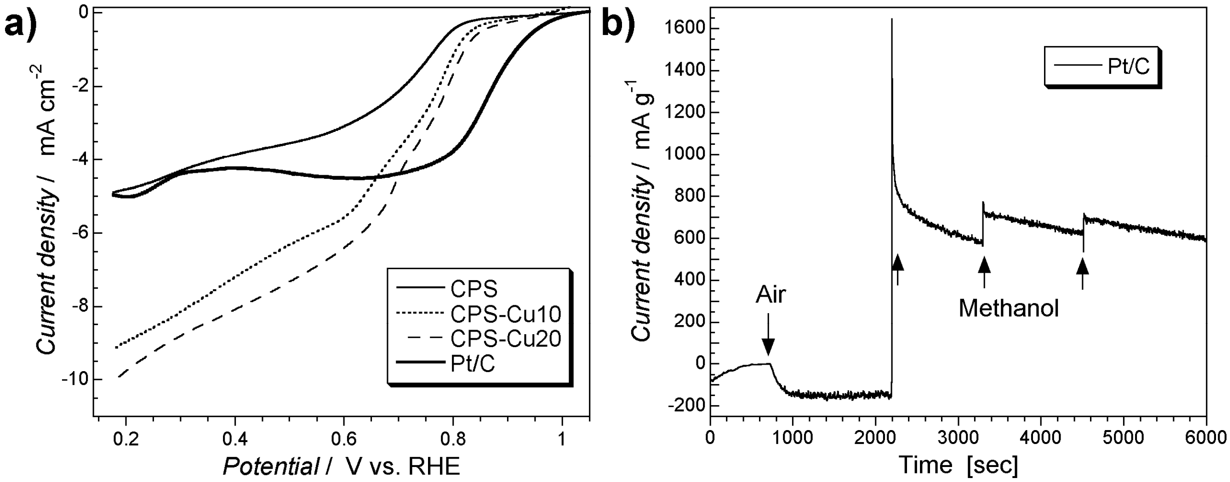

Fig. 5. a) Linear sweep voltammograms on the modified glassy carbon RDE in air-saturated 0.1 M KOH at 2000 rpm and scan rate of 5 mV s^{-1} for the materials studied compared to 20% Pt on Vulcan XC72; b) Chronoamperometric response for 20% Pt on Vulcan XC-72 at 0.73 V.

3.2. Characterization of carbon/graphene/copper hybrid materials

Thermal analysis in air (Fig. S2 of ESI), when all carbonaceous phase is expected to be burned off and inorganic copper salts (carbonates, sulfates or sulfides) converted to copper oxide, indicates that the content of copper in CPS-Cu10 and CPS-Cu20 is 4.56 wt. % and 9.60 wt. %, respectively. This is in agreement with the intended difference in the copper content in both composites. Assuming that the content of copper would be equal to that on the surface it translates to 0.85 at. % and 1.76 at. % for CPS-Cu10 and CPS-Cu20, respectively.

The atomic concentration (%) of elements on the surface measured by XPS is presented in Table 1. Apparently carbonization of the polymer in the presence of Cu(II) from the Cu-BTC phase results in an increase in the content of sulfur on the surface. We link that increase to the formation of copper sulfide/sulfates during thermal decomposition of sulfonic groups and the reduction of sulfur by the carbon phase.[46] Interestingly, the content of oxygen on the surface decreases with an increase in the copper content which might suggest more copper/sulfur in reduced forms on CPS-Cu20 than those on CPS-Cu10. The comparison of the content of copper on the surface to its content in the bulk indicates that in the case of CPS-Cu10 more copper is accumulated on the surface than in the bulk while for CPS-Cu20 an opposite trend is found.

Table 1. Atomic concentration (%) of elements on the surface for the materials studied.

Sample	XPS analysis (at. %)				EDX analysis (at. %)			
	C	O	S	Cu	C	O	S	Cu
[a]CPS	87.4	12.1	0.5	---	86.2	13.2	0.6	---
CPC-Cu10	88.3	9.6	1.1	1.0	86.3	11.2	1.2	1.3
CPS-Cu20	88.9	8.8	0.9	1.3	86.9	9.8	1.4	1.9

[a]Content of elements from XPS analysis for CPS carbon reintroduced from Reference.[58]

The deconvoluted C 1*s*, O 1*s*, S 2*p* and Cu $2p_{3/2}$ core level spectra are collected in Fig. S3 of ESI. Table 2 summarizes the results of the deconvolution with the assignment of the binding energies to specific species present on the surface. The comparison of the deconvolution C 1*s* core energy levels for both catalysts indicates the close similarity in the chemistry of both carbon phases with about 25 % of carbon atoms in sp^2 configurations. In those, the carbon oxygen bonds in phenol, ether and alcohol groups predominate. The differences are seen in the configuration of oxygen species. Based on combined deconvolutions of C 1*s* and O 1*s* core energy levels, the results suggest that CPS-Cu20 has more oxygen bound to copper either in oxide or salts than has the CPS-Cu10 sample. The analysis of Cu $2p_{3/2}$ and S 2*p* confirms this showing the majority of copper bound to oxysulfur on high oxidation states (168.8 eV and 935.4 eV[56]) in the case of the former sample. On the other hand, on the surface of CPS-Cu10, even though the majority of copper is also bound to oxysulfur, the contribution of thiols and sulfides (at 164.2 eV and 932.6 eV[56, 57]) is clearly visible.

The chemistry of the polymer derived carbon, CPS, has been analyzed by XPS previously[58] and the results show that more carbon is in sp^2 configurations than that in the composites. It is owing to the carbons phase from the MOF/GO components in the latter samples. Interestingly, the addition of copper results in less oxygen atoms on the surface, which should increase the hydrophobicity level. Sulfur atoms on the surface of CPS carbon are equally distributed between reduced and oxidized forms. Sulfur atoms in thiophenic configurations incorporated to the carbon matrix can contribute to ORR activity found on this carbon.[10, 12, 43]

Table 2. The results of deconvolution of C 1*s*, O 1*s*, S 2*p* and Cu 2*p*$_{3/2}$ core level spectra.

Energy, eV	Bond assignment	^{a}CPS	CPS-Cu10	CPS-Cu20
C 1*s*				
284.8	C-C (graphitic carbon in sp^2 configuration)	86.0	73.4	73.7
286.2	C-(O, S, H) (phenolic, alcoholic, etheric)	10.2	14.6	14.4
287.3	C=O (carbonyl or quinone)		6.3	6.0
288.7	O-C=O (carboxyl or ester)	3.8	3.5	3.4
290.1	$\pi-\pi^*$		2.2	2.5
O 1*s*				
532.0	O=C/O=S (in carboxyl/carbonyl or sulfoxides/sulfones, sulfinyls, or oxygen in copper oxide and oxysulfur salts)	22.7	64.5	64.3
533.4	O-C/O-S (in phenol/epoxy or thioesters/sulfonic, or OH$^-$)	64.3	35.5	35.7
536.6	Oxygen atoms in water or chemisorbed oxygen species	12.8		
S 2*p*				
164.2	-SH (in thiols, bisulfides, Cu_xS_y)	50.0	43.3	32.4
167.9	R_2-S=O/R-SO_2-R (in sulfoxides, sulfones); R-SO_3H (in sulfonic acids)	50.0		
168.8	R-SO_3H/SO_4^{2-} (in sulfonic acids, sulphate)		56.7	67.6
Cu 2*p*$_{3/2}$				
932.6	Cu_xS_y		6.3	6.5
935.4	$CuSO_4$ and $Cu(OH)_2$		93.7	93.5

^{a}XPS results for CPS carbon reintroduced from Reference.[58]

X-Ray diffraction patterns (Fig. 6), besides broad humps related to the carbon phase show the sharp peaks at 42.09, 43.64, 49.09 and 51.13° which correspond to the hexagonal structure of graphitic units and suggest some order in the carbon phase.[59] The composites show crystallographic phase of copper oxide at 35.49 and 43.59°.[60] The intensities of these peaks increase with an increase in the content of copper in the samples. Moreover, the peaks at 13.81, 16.46, 22.68 and 25.88° visible in the diffraction pattern for CPS-Cu20 are assigned to the presence of copper hydroxide sulfate monoclinic-phase.[61]

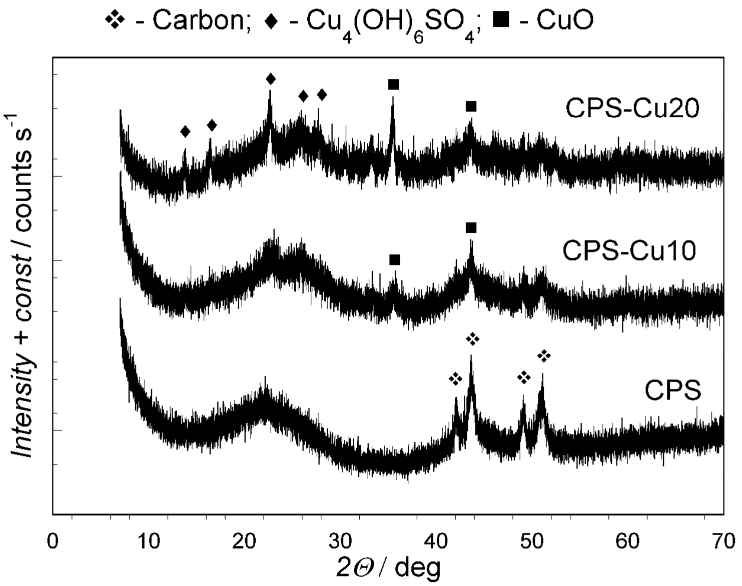

Fig. 6. X-Ray diffraction patterns for the materials studied.

The DTG curves for the composites presented in Fig. 7 show the peaks between 180 – 220 °C representing the decomposition of copper sulfite and removal of water from crystalline sulfates,[62] and the decomposition of various copper sulfates and carbonates at 350 °C.[62] The peak at 900 °C is linked to the reduction of copper by the carbon phase[63] and an onset of the large weight loss at temperature higher than 1000 °C indicates the presence of copper sulfides, Cu_xS_y.[62] As expected based on the XPS results, all sulfur containing copper salts are in greater quantities in CPS-Cu20 than those in CPS-Cu10. Interestingly, the reduction of copper from Cu^{2+} to Cu^{+} is clearly seen at 900 °C only for the former sample.

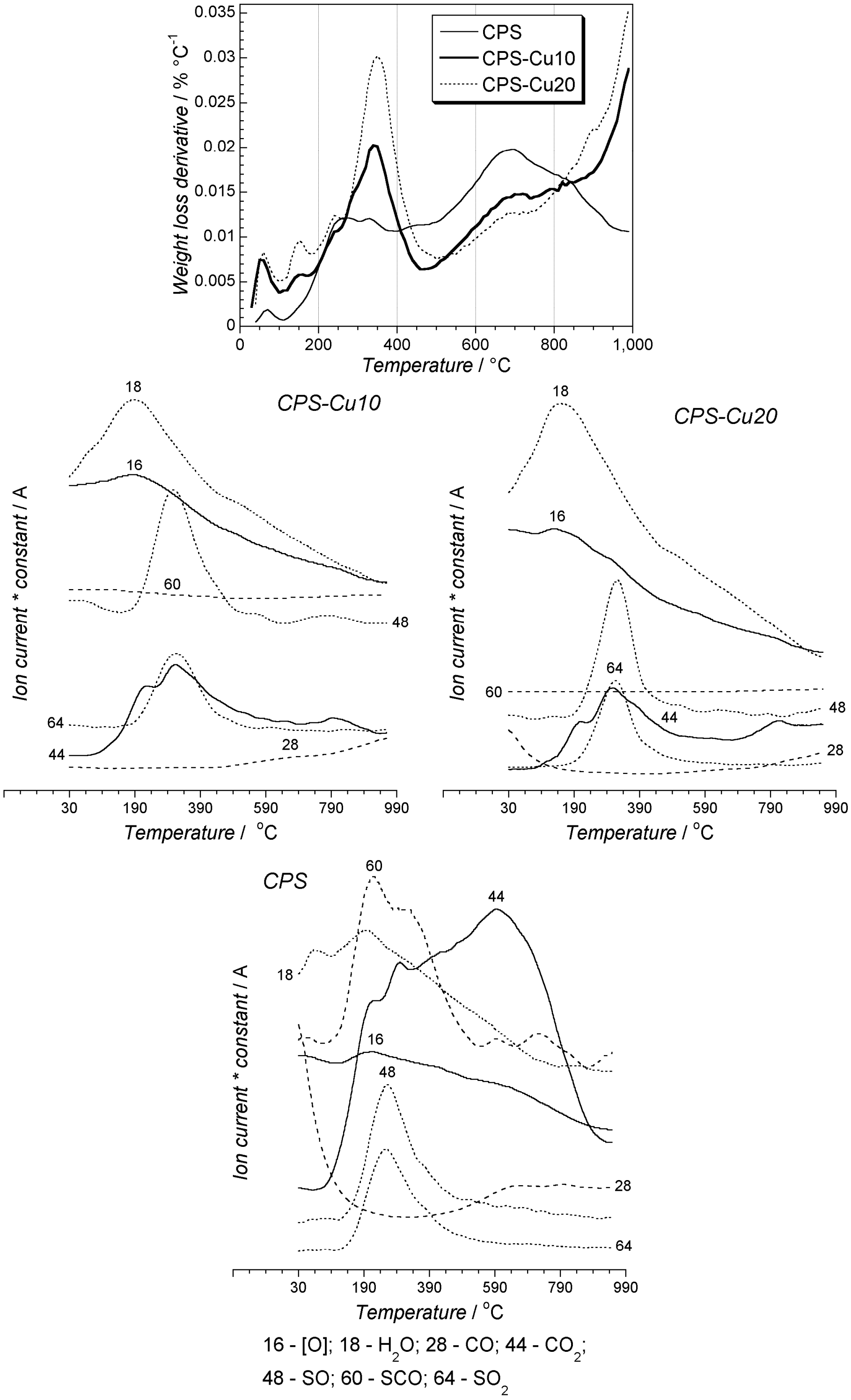

Fig. 7. DTG curves in helium and *m/z* thermal profiles.

The *m/z* thermal profiles obtained from the MS analysis of the decomposition products are collected in Fig. 7. The initial carbon shows the removal of H_2O (*m/z* 18), CO_2 (*m/z* 44) and CO (*m/z* 28) representing the decomposition of carboxylic acids at low temperature and quinone, carbonyl, lactone, phenol and ether functional groups at temperatures higher than 400 ^oC.[63] Release of SO_2 (*m/z* 64) and SO (*m/z* 48) at about 260 ^oC is from the decomposition of sulfoxides, sulfones and sulfonic acids.[64] SCO (*m/z* 60) is released as a complex pattern from more reduced sulfur species incorporated to the carbon matrix.

The *m/z* profiles for the composites change and they show the carbon phase in a more reduced state than that in CPS. The removal of water from hydrated inorganic salts is clearly visible at 180 ^oC, SO_2 and SO thermal profiles from decomposition of oxysulfur copper salts show maxima at 350 ^oC. Interestingly, the peaks representing the decomposition of oxysulfur copper salts are broader for CPS-Cu10 than those for CPS-Cu20. This is in agreement with the XPS results (Table 2).

The SEM images presented in Fig. 8a-f clearly show the inorganic phase on the surface of the copper containing composites as crystals of well-defined geometric shapes. Based on XRD results we link them to copper hydroxide sulfate (Brochantite). It is evident that the crystals are larger and more visible on the surface of CPS-Cu20 than on that of CPS-Cu10. Moreover, the copper species of a small particle size (2-5 nm) evenly distributed/embedded in carbon network are visible TEM (Fig. 8g-i) and HR-TEM (Fig. 8j-l) images. Based HR-TEM images measured lattice fringe distance is 0.247 nm, corresponding to monoclinic-phase $Cu_4(OH)_6SO_4$ or CuO. The small size of particles on the surface of the composites can play an important role in the electrocatalytic activity for ORR. The graphene phase is not visible in the morphology of the composites likely owing to its small content and embedding within the nanoporous carbon phase. In fact its content should be only about 1-2 wt. %. From the point of the carbon support texture, the similarities are seen and they are linked to the mechanism of polymer carbonization.[46]

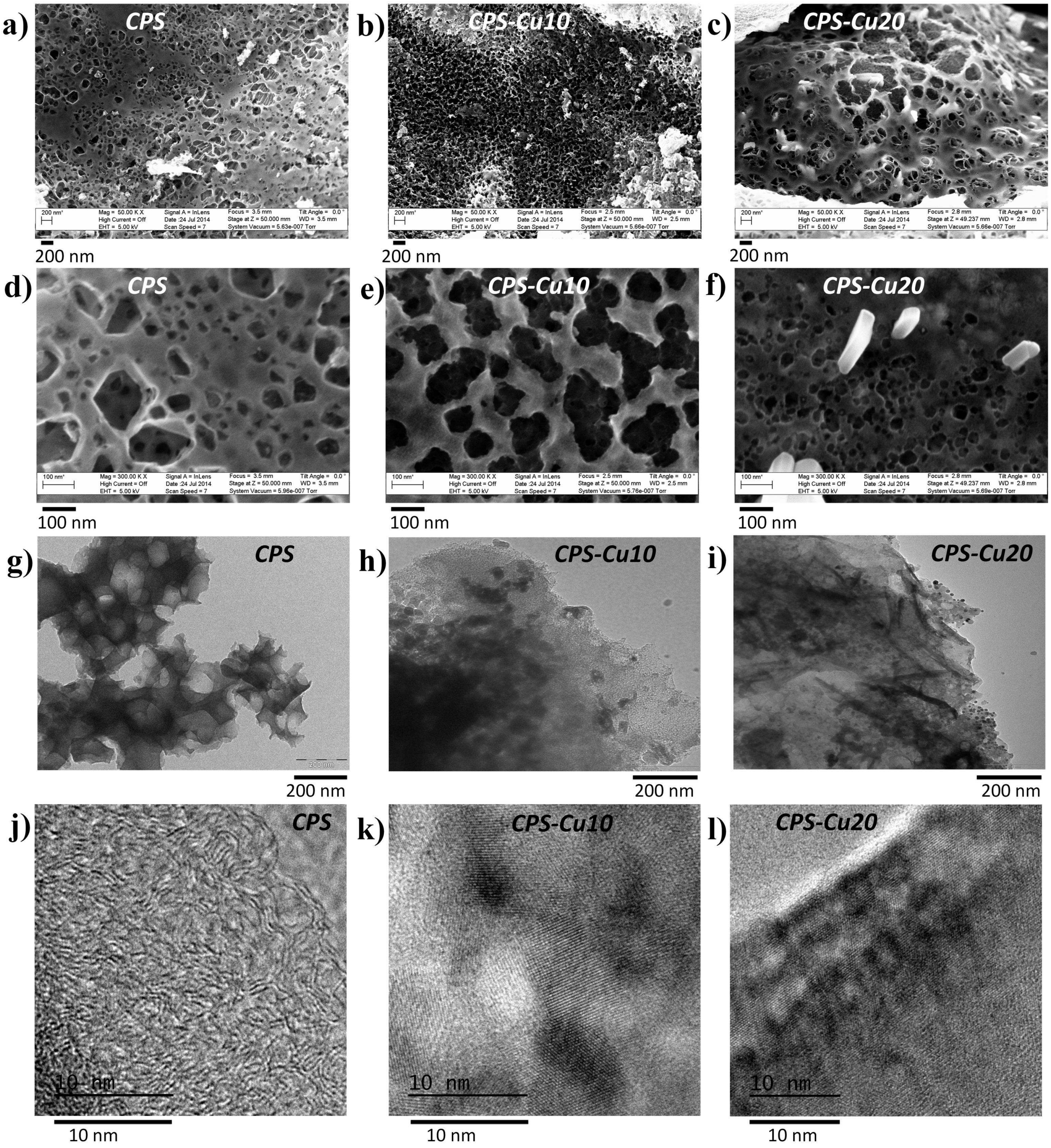

Fig. 8. Texture characterization of the materials studied: a-f) SEM; g-i) TEM; and j-l) HR-TEM images, respectively.

Even though our materials are not tested as adsorbents in the traditional meaning of this word their porosity might be a very important aspect affecting the efficiency of ORR. For this process oxygen molecules have to be attracted to the surface. The factors, which might enhance it, are the size and volume of small pores, surface chemistry and surface hydrophobicity.[65-67] Evaluation of the later indicates that with an increase in the content of copper the hydrophobicity level, defined as a ratio of the amount of benzene to water adsorption, visibly increases (Table 3). This can be related to the presence of copper sulfides.[68] The hydrophobic surface in pores similar in the size to the oxygen molecule (0.346 nm[69]) would enhance oxygen withdrawal from the electrolyte solution and its adsorption on the active catalytic centers.[67]

The nitrogen adsorption isotherms and pore size distributions are presented in Fig. 9. The parameters of the pore structure calculated from the isotherms are collected in Table 3. Even though the surface area of the composites decreased up to 30% compared to that for CPS some extent of this trend could be linked to mass dilution effect caused by an introduction of the heavy, nonporous inorganic phases. The evaluation of porosity indicates that the volume of small pores, less than 1.0 and 0.7 nm decreased. This effect is especially visible for the composite with higher content of copper where $V_{<0.7\ nm}$ decreased 21 % compared to the volume of these pores in CPS carbon. Moreover, a marked increase in the volume of mesopores is found, which are desired features facilitating O_2 transport to the small pores where catalytic centers might exist. These changes undoubtedly reflect in an increase in the capacitive effect seen on the CV curves (Fig. 1). These new pores, existing likely on the interface between the graphene phase and copper-based phase, might create specific centers and are important in the cathodic reduction of O_2. The CPS carbon component with a well developed porous texture provides a high dispersion of these centers. This led to the much higher current than those found for the catalyst obtained from the MOF/GO composites which were considered as rather nonporous materials.[38] In those materials, a specific architecture of metallic copper/copper oxides distributed on a conductive graphene phase was indicated as enhancing the activity for ORR. In the case of the composites addressed in this paper the carbon support along with the highly dispersed graphene phase also provides the conductive path for the electrons.

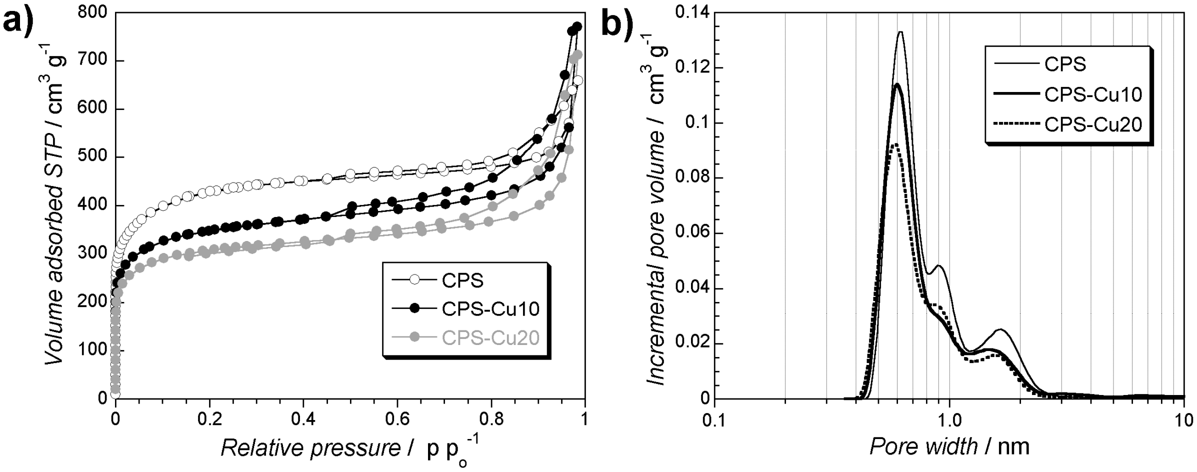

Fig. 9. a) N_2 adsorption isotherms at -196 ^{o}C and b) pore size distribution of the materials studied.

Table 3. The parameters of porous structure calculated from nitrogen adsorption measurements, the amounts of water and benzene adsorbed and hydrophobicity level (HL), and the samples' conductivity (σ).

Sample	S_{BET} (m^2 g^{-1})	S_{NLDFT} (m^2 g^{-1})	V_t (cm^3 g^{-1})	V_{meso} (cm^3 g^{-1})	V_{mic} (cm^3 g^{-1})	$V_{<0.7nm}$ (cm^3 g^{-1})	$V_{<1nm}$ (cm^3 g^{-1})	V_{mic}/V_t	H_2O (wt. %)	C_6H_6 (wt. %)	HL	σ (S m^{-1})
CPS	1416	1470	1.019	0.429	0.590	0.228	0.375	0.58	35.50	18.92	0.53	20.1
CPS-Cu10	1153	1269	1.193	0.722	0.471	0.210	0.314	0.40	28.53	16.70	0.59	40.0
CPS-Cu20	1017	1135	1.102	0.679	0.423	0.180	0.284	0.38	24.56	15.98	0.65	42.9

In explaining the higher catalytic activity of our composites than those reported previously[38] the surface chemistry has to be taken into consideration. Even though the XPS results show that oxysulfur copper salts are the predominant inorganic phases, the relative surface concentration of sulfide (Cu_xS_y) and reduced sulfur is higher on the surface of CPS-Cu10 than that on CPS-Cu20. It has been recently reported that $Cu_{2-x}S_y$ species in conjunction with the oxygen functionalized carbon nanodots exhibited catalytic activity for ORR in acidic electrolytes.[70] The higher contribution of copper sulfides in the CPS-Cu10 composite than that in CPS-Cu20 might explain its higher number of electron transfer at more negative potential and higher kinetic current density. The reduced sulfur and copper sulfides, along with the higher surface area and porosity of CPS-Cu10 than those of CPS-Cu20 might be also responsible for a marked increase in the kinetic current density of the former sample in comparison with that on CPS. Moreover, in the case of CPS-Cu10 the results of the chemical analysis suggest that active copper might be better utilized than that on CPS-Cu20 since it is uniformly distributed on the surface and in the bulk of the composite. In the latter sample, the bulk of the material contains more copper than does the surface. These copper sulfides are known of hydrophobicity[68] and thus should have high affinity to adsorb oxygen.[67] On the other hand, on the CPS-Cu20 catalyst only a small increase in a recorded kinetic current density was found compared to that on CPS-Cu10 and this increase cannot be linked directly to the differences in the content of copper. Nevertheless, the highest current generated on the CPS-Cu20 might be governed by more active copper sulfide sites on the surface in absolute quantity than those on CPS-Cu10. The highest electric conductivity of this sample (Table 3) can also contribute to this effect. The oxygen reduction activity of the carbon phase itself is linked to the content of sulfur in the reduced form[10] and a high volume of pores less than 0.7 nm.[43]

As indicate above, our materials are complex and we link their good performance as ORR catalysts to the synergistic features of their surfaces and effect of Cu_xS_y. Owing to the interplay of various factors it is hard to imitate the systems on a less complex level. Nevertheless, to check the effect of CuS activity, CPS carbon was physically mixed with 2 wt. % CuS and tested as ORR catalyst (Fig. S4). The results indicated a small but consistent increase in the number of electron transfer and kinetic current density supporting the activity of CuS addressed by Shih and coworkers.[70] It has to be mentioned here that the strong effect was not expected since a physical mixture was not able to provide important features such as specific chemistry of copper sulfide, its high dispersion in the micropore system or an enhanced electric conductivity. More studies are needed to better understand and fully used these complex nanoporous carbon/copper species systems.

4. Conclusions

The results presented in this paper show that the combination of the sulfur containing polymer, and highly dispersed copper in Cu-BTC composite with GO, followed by carbonization at 800 ^{o}C led to a well performing oxygen reduction catalyst in alkaline media. Release of hydrogen sulfide during carbonization, was evident by its characteristic smell of the final materials. Its presence resulted in the deposition of copper sulfides, which are considered as attracting oxygen and promoting electron transfer through carbonaceous phase consisting carbon with well distributed graphene phase. The number of electron transfer over 3ē at potential 0.68 V vs. RHE indicating a high efficiency of ORR. The high kinetic current density of 30 mA cm^{-2} was also measured at the potential 0.18 V vs. RHE. The porosity of the catalysts was found of paramount importance since a high surface area provides a high dispersion of the active phases. Very small pores with hydrophobic surface governed by the presence of copper sulfides and sulfur in C-S configurations attract oxygen molecules from the electrolyte.

Acknowledgement

This research was partially supported by Ministerio de Innovación y Ciencia CTQ2012-37925-C03-03, FEDER funds, and Project of Excellence RNM 1565 of Junta de Andalucía.

Electronic Supplementary Information (ESI)

Characterization of the prepared materials by XPS, thermogravimetric analysis in air and Koutecky–Levich (K-L) plots at different potential values.

References

1. B. C. H. Steele and A. Heinzel, *Nature*, 2001, **414**, 345-352.
2. V. R. Stamenkovic, B. Fowler, B. S. Mun, G. Wang, P. N. Ross, C. A. Lucas and N. M. Markovic, *Science*, 2007, **315**, 493-497.
3. M. Liu, R. Zhang and W. Chen, *Chem. Rev.*, 2014, **114**, 5117-5160.
4. Y. Li, W. Zhou, H. Wang, L. Xie, Y. Liang, F. Wei, J.-C. Idrobo, S. J. Pennycook and H. Dai, *Nat. Nanotechnol.*, 2012, **7**, 394-400.
5. K. P. Gong, F. Du, Z. H. Xia, M. Durstock and L. M. Dai, *Science*, 2009, **323**, 760-764.

6. S. Yang, L. Zhi, K. Tang, X. Feng, J. Maier and K. Mullen, *Adv. Funct. Mater.*, 2012, **22**, 3634-3640.
7. Z. Yang, Z. Yao, G. Li, G. Fang, H. Nie, Z. Liu, X. Zhou, X. Chen and S. Huang, *ACS Nano*, 2012, **6**, 205-211.
8. T. Palaniselvam, H.B. Aiyappa and S. Kurungot, *J. Mater. Chem.*, 2012, **22**, 23799-23805.
9. C. Zhang, R. Hao, H. Lian and Y. Hou, *Nano Energy*, 2013, **2**, 88-97.
10. J. Liang, Y. Jiao, M. Jaroniec and S.Z. Qiao, *Angew. Chem.*, 2012, **124**, 11664-11668; *Angew. Chem. Int. Ed.*, 2012, **51**, 1-6.
11. J. Liang, Y. Zheng, J. Chen, J. Liu, D. Hulicova-Jurcakova, M. Jaroniec and S. Z. Qiao, *Angew. Chem.*, 2012, **124**, 3958-3962; *Angew. Chem. Int. Ed.*, 2012, **51**, 3892-3896.
12. M. Seredych and T.J. Bandosz, *Carbon*, 2014, **66**, 227-233.
13. R.-S. Zhong, Y.-H. Qin, D.-F. Niu, J.-W. Tian, X.-S. Zhang, X.-G. Zhou, S.-G. Sun and W.-K. Yuan, *J. Power Sour.*, 2013, **225**, 192-199.
14. L. Wang, A. Ambrosi and M. Pumera, *Angew. Chem.*, 2013, **125**, 14063-14066; *Angew. Chem. Int. Ed.*, 2013, **52**, 13818-13821.
15. Y. Zheng, Y. Jiao, J. Chen, J. Liu, J. Liang, A. Du, W. Zhang, Z. Zhu, S. C. Smith, M. Jaroniec, G.Q.M. Lu and S. Z. Qiao, *J. Am. Chem. Soc.*, 2011, **133**, 20116-20119.
16. Y. Zhang, M. Chu, L. Yang, W. Deng, Y. Tan, M. Ma and Q. Xie, *Chem. Commun.,* 2014, **50**, 6382-6385.
17. L. An, W. Huang, N. Zhang, X. Chen and D. Xia, *J. Mater. Chem. A*, 2014, **2**, 62-65.
18. J. Wu, Z. Yang, X. Li, Q. Sun, C. Jin, P. Strasser and R. Yang, *J. Mater. Chem. A*, 2013, **1**, 9889-9896.

19. E. Antolini, *Appl. Catal. B: Environ.*, 2009, **88**, 1-24.

20. M. Lefevre, E. Proietti, F. Jaouen and J.-P. Dodelet, *Science*, 2009, **324**, 71-74.

21. G. Wu, K. L. More, C. M. Johnston and P. Zelenay, *Science*, 2011, **332**, 443-447.

22. V. J. Watson, C. N. Delgado and B. E. Logan, *Environ. Sci. Technol.*, 2013, **47**, 6704-6710.

23. C. H. Choi, S. H. Park and S. Woo, *ACS Nano*, 2012, **6**, 7084-7091.

24. D. Deak, E. J. Biddinger, K. Luthman and U. S. Ozkan, *Carbon*, 2010, **48**, 3637-3659.

25. M. Zhong, E.K. Kim, J.P. McGann, S.-E. Chun, J.F. Whitacre, M. Jaroniec, K. Matyjaszewski and T. Kowalewski, *J. Am. Chem. Soc.*, 2012, **134**, 14846-14857.

26. S. Wang, L. Zhang, Z. Xia, A. Roy, D. W. Chang, J.-B. Baek and L. Dai, *Angew. Chem. Int. Ed.*, 2012, **51**, 4209-4212.

27. C. H. Choi, M. W. Chung, H. C. Kwon, S. H. Park and S. I. Woo, *J. Mater. Chem. A*, 2013, **1**, 3694-3699.

28. H. Li, W. Kang, L. Wang, Q. Yue, S. Xu, H. Wang and J. Liu, *Carbon*, 2013, **54**, 249-257.

29. J. D. Wiggins-Camacho and K. J. Stevenson, *J. Phys. Chem. C*, 2011, **115**, 20002-20010.

30. L. Li, S.-H. Chai, S. Dai and A. Manthiram, *Energy Environ. Sci.*, 2014, **7**, 2630-2636.

31. J. B. Xu, P. Gao and T. S. Zhao, *Energy Environ. Sci.*, 2012, **5**, 5333-5339.

32. S. Guo, S. Zhang and S. Sun, *Angew. Chem.*, 2013, **125**, 8686-8705; *Angew. Chem. Int. Ed.*, 2013, **52**, 8526-8544.

33. M. Jahan, Z. Liu and K.P. Loh, *Adv. Funct. Mater.*, 2013, **23**, 5363-5372.

34. S. Ma, G.A. Goenaga, A.V. Call and D.-J. Liu, *Chem. Eur. J.*, 2011, **17**, 2063-2067.

35. M. Jahan, Q. Bao and K. P. Loh, *J. Am. Chem. Soc.*, 2012, **134**, 6707-6713.

36. S. Pandiaraj, H. B. Aiyappa, R. Banerjee and S. Kurungot, *Chem. Commun.*, 2014, **50**, 3363-3366.
37. J. Li, Y. Chen, Y. Tang, S. Li, H. Dong, K. Li, M. Han, Y.-Q. Lan, J. Bao and Z. Dai, *J. Mater. Chem. A*, 2014, **2**, 6316-6319.
38. C. O. Ania, M. Seredych, E. Rodriguez-Castellon and T. J. Bandosz, *Appl. Catal. B: Environ.*, 2015, **163**, 424-435.
39. Z. Chen and T.J. Meyer, *Angew. Chem.*, 2013, **125**, 728-731; *Angew. Chem. Int. Ed.*, 2013, **52**, 700-703.
40. Z. Chen, P. Kang, M.-T. Zhang, B.R. Stoner and T.J. Meyer, *Energy Environ. Sci.*, 2013, **6**, 813-817.
41. R. Zhou, Y. Zheng, D. Hulicova-Jurcakova and S.Z. Qiao, *J. Mater. Chem. A*, 2013, **1**, 13179-13185.
42. C. Petit, J. Burress and T.J. Bandosz, *Carbon*, 2011, **49**, 563-572.
43. M. Seredych, E. Rodríguez-Castellón, M. J. Biggs, W. Skinner and T. J. Bandosz, *Carbon*, 2014, **78**, 540-558.
44. M.D. Allendorf, A. Schwartzberg, V. Stavila and A.A. Talin, *Chem. Eur. J.*, 2011, **17**, 11372-11388.
45. S. S.-Y. Chui, S. M.-F. Lo, J. P. H. Charmant, G. Orpen and I. D. Williams, *Science*, 1999, **283**, 1148-1150.
46. D. Hines, A. Bagreev and T. J. Bandosz, *Langmuir*, 2004, **20**, 3388-3397.
47. J. Jagiello and J. P. Olivier, *Adsorption*, 2013, **19**, 777-783.
48. S. Poulston, P.M. Parlett, P. Stone and M. Bowker, *Surf. Interface Anal.*, 1996, **24**, 811-820.

49. M. Jayalakshmi and K. Balasubramanian, *Int. J. Electrochem. Sci.*, 2008, **3**, 1277-1287.

50. J.M.M. Droog, C.A. Alderliesten, P.T. Alderliesten and G.A. Bootsma, *J. Electroanal. Chem. Interfacial Electrochem.*, 1980, 111, 61-70.

51. Y. Wan, X. Wang, H. Sun, Y. Li, K. Zhang and Y. Wu, *Int. J. Electrochem. Sci.*, 2012, **7**, 7902-7914.

52. F. Hasche, M. Oezaslan and P. Strasser, *ChemPhysChem*, 2012, **13**, 828-834.

53. J. H. Bang, K. Han, S. E. Skrabalak, H. Kim and K. S. Suslick, *J. Phys. Chem. C*, 2007, **111**, 10959-10964.

54. X.-Y. Yan, X.-L. Tong, Y.-F. Zhang, X.-D. Han, Y.-Y. Wang, G.-Q. Jin, Y. Qin and X.-Y. Guo, *Chem. Commun.*, 2012, **48**, 1892-1894.

55. J. Qiao, L. Xu, L. Ding, P. Shi, L. Zhang, R. Baker and J. Zhang, *Int. J. Electrochem. Sci.*, 2013, **8**, 1189-1208.

56. B. R. Strohmeier, D. E. Levden, R. S. Field and D. M. Hercules, *J. Catal.*, 1985, **94**, 514-530.

57. K. Uvdal, P. Bodo and B. Liedberg, *J. Colloid Interf. Sci.*, 1992, **149**, 162-173.

58. C. Petit, K. Kante and T.J. Bandosz, *Carbon*, 2010, **48**, 654-667.

59. J. Howe, C. Rawn, L. Jones and H. Ow, *Powder Diffraction*, 2003, **18**, 150-154.

60. S. Elzey, J. Baltrusaitis, S. Bian and V.H. Grassian, *J. Mater. Chem.*, 2011, **21**, 3162-3169.

61. R. Ma, J. Stegemeier, C. Levard, J.G. Dale, C.W. Noack, T. Yang, G.E. BrownJr. and G.V. Lowry, *Environ. Sci.: Nano*, 2014, **1**, 347-357.

62. Weast, R.C.; Astle, M.J. In *Handbook of Chemistry and Physics*, 62nd-edn; Weast, R.C., Astle, M.J., Eds.; CRC Press: Boca Raton, Florida, **1981**; p B-99.

63. J.L. Figueiredo, M.F.R. Pereira, M.M.A. Freitas and J.J.M. Órfão, *Carbon*, 1999, **37**, 1379-1389.
64. X. Zhao, Q. Zhang, C.-M. Chen, B, Zhang, S. Reiche, A. Wang, T. Zhang, R. Schlogl and D. S. Su, *Nano Energy*, 2012, **1**, 624-630.
65. J. Guo, J.R. Morris, Y. Ihm, C.I. Contescu, N.C. Gallego, G. Duscher, S.J. Pennycook and M.F. Chisholm, *Small*, 2012, **8**, 3283-3288.
66. V.V. Strelko, N.T. Kartel, I.N. Dukhno, V.S. Kuts, R.B. Clarkson and B.M. Odintsov, *Surf. Sci.*, 2004, **548**, 281-290.
67. D. A. Doshi, E. B. Watkins, J. N. Israelachvili and J. Majewski, *PNAS*, 2005, **102**, 9458-9462.
68. G. Hangone, D. Bradshaw and Z. Ekmekci, *J. South Afr. Inst. Min. Metall.*, 2005, **105**, 199-206.
69. I. P. O'koye, M. Benham and K. M. Thomas, *Langmuir*, 1997, **13**, 4054-4059.
70. Z.-Y. Shih, A. P. Periasamy, P.-C. Hsu and H.-T. Chang, *Appl. Catal. B: Environ.*, 2013, **132-133**, 363-369.

Caption to the Tables

Table 1. Atomic concentration (%) of elements on the surface for the materials studied.

Table 2. The results of deconvolution of C 1*s*, O 1*s*, S 2*p* and Cu $2p_{3/2}$ core level spectra.

Table 3. The parameters of porous structure calculated from nitrogen adsorption measurements, the amounts of water and benzene adsorbed and hydrophobicity level (HL), and the samples' conductivity (σ).

Captions to the Figures

Fig. 1. Cyclic voltammograms on modified glassy carbon RDE in air-saturated 0.1 M KOH at scan rate of 5 mV s^{-1} for the (a) polymer-derived carbon, (b and c) copper/carbon composites and (d) 20% Pt on Vulcan XC-72.

Fig. 2. Linear sweep voltammograms on modified glassy carbon RDE in air-saturated 0.1 M KOH at different rotation speeds and scan rate of 5 mV s^{-1} for the (a) polymer-derived carbon, (b and c) copper/carbon composites and (d) 20% Pt on Vulcan XC-72. LSV for oxygen reduction reaction was corrected for capacitive currents contribution.

Fig. 3. a) Number of electron transfer versus potential; b) comparison of the kinetic current density.

Fig. 4. a) Chronoamperometry for methanol tolerance at the potential 0.73 V; b) Stability testing by cycling at 0.73 V.

Fig. 5. a) Linear sweep voltammograms on the modified glassy carbon RDE in air-saturated 0.1 M KOH at 2000 rpm and scan rate of 5 mV s^{-1} for the materials studied compared to 20% Pt on Vulcan XC72; b) Chronoamperometric response for 20% Pt on Vulcan XC-72 at 073 V.

Fig. 6. X-Ray diffraction patterns for the materials studied.

Fig. 7. DTG curves in helium and *m/z* thermal profiles.

Fig. 8. Texture characterization of the materials studied: a-f) SEM; g-i) TEM; and j-l) HR-TEM images, respectively.

Fig. 9. a) N_2 adsorption isotherms at -196 ^{o}C and b) pore size distribution of the materials studied.